ELSEVIER

Spectrochimica Acta Part A 58 (2002) 629–647

SPECTROCHIMICA ACTA PART A

www.elsevier.com/locate/saa

A realistic double many-body expansion potential energy surface for $SO_2(\tilde{X}^1A')$ from a multiproperty fit to accurate ab initio energies and vibrational levels

A.J.C. Varandas *, S.P.J. Rodrigues

Departamento de Química, Universidade de Coimbra, 3004-535 Coimbra, Portugal

Received 22 August 2001; accepted 6 September 2001

Abstract

A single-valued double many-body expansion potential energy surface (DMBE I) recently obtained for the ground electronic state of the sulfur dioxide molecule by fitting correlated ab initio energies suitably corrected by scaling the dynamical correlation energy is now refined by fitting simultaneously available spectroscopic levels up to 6886 cm^{-1} above the minimum. The topographical features of the novel potential energy surface (DMBE II) are examined in detail, and the method is emphasized as a robust route to fit together state-of-the-art theoretical calculations and spectroscopic measurements using a single fully dimensional potential form.

Keywords: Potential energy surface; Multiproperty fit; Ab initio energies and vibrational levels

1. Introduction

Sulfur containing molecules are well known to play an important role in environmental chemistry. In particular, sulfur dioxide is known to be one of the major air pollutants released to the atmosphere as a result of volcanic eruptions and fuel combustion in human activities. It contributes to the generation of smog and constitutes a serious health hazard for the respiratory system [1]. It is also a major source of acid rain after its oxidation and reaction with water in the atmosphere. Yet, its role in the combustion of sulfur containing materials [2], atmospheric photochemistry [1], and dynamics remains ubiquitous. It comes therefore as no surprise that SO_2 has been the subject of intense study. Of special relevance here is its rovibrational spectroscopy, which has been extensively investigated, both experimentally [3–10] and theoretically [11–14]. Clearly, the experimental rovibrational work goes back almost fifty years ago [3], with the more recent studies being perhaps those of Yamanouchi and coworkers [7,8] who have identified a large number of highly excited vibrational levels between 17300 and 22500 cm^{-1} and assigned many of such levels

* Corresponding author. Fax: +351-39-827-703.
E-mail address: varandas@qtvs1.qui.uc.pt (A.J.C. Varandas).

1386-1425/02/$ - see front matter
PII: S1386-1425(01)00661-8

using a Dunham-type expansion. One should also mention that studies on the predissociation mechanism of the title molecule have been reported [15,16]. In addition, the SO_2 molecule has provided an important prototype system for the study of vibration–rotation interactions and the onset of classical chaos [17–19], while offering also a testing ground for work on normal to local mode transitions and quantum stochasticity [12].

From the point of view of ab initio electronic structure calculations, studies have been reported both for the ground and excited states of the title molecule [15,20–26]. However, the only realistic global function for the title system which stems from a least-squares fit to accurate ab initio data is the DMBE I potential energy surface reported recently by the present authors and Sabín [27] using the double many-body expansion [28,29] method. In fact, several analytical representations of the ground state SO_2 potential energy surface have been suggested but they all stem mostly from fits to rovibrational spectroscopic data [14,30–34]. Indeed, only two potential functions have been constructed for SO_2 from fits to ab initio energies [35,36]. Furthermore, one of those remains unpublished and is valid only over limited ranges of the molecule configurational space (see Refs. [19,37])

The adiabatic potential energy surface of ground state SO_2 shows [20,24], similar to O_3, four minima. The one lying lowest in energy corresponds to the equilibrium C_{2v} structure of SO_2. Considerably higher in energy lie two other equivalent minima corresponding to superoxide SOO structures. These refer to species having C_s symmetry, and are related through permutation of the two oxygen atoms. All these three minima lie on the same ($^1A'$, $^1A_1$) potential energy surface. The fourth minimum is associated with a ring structure of C_{2v} symmetry in which the OO distance is smaller than the SO ones [20,24], being the analog of the cyclic isomeric structure of O_3. Such a minimum belongs to another electronic state of the same symmetry ($^1A'$, $^1A_1$) which is known to cross the previous one, although its exact locus has not been determined thus far.

The paper has the following structure. In Section 2, we survey briefly the ab initio energies used for the calibration procedure, and which have been previously employed to construct the SO_2 DMBE I potential energy surface [27]. A brief description of the DMBE formalism is then presented in Section 3, while the technical details concerning the multiproperty least-squares fitting procedure are in Section 4. Besides the ab initio energies mentioned above, the fitted data include many accurately measured experimental vibrational levels for SO_2. Moreover, since no rotational data is employed and the ab initio equilibrium geometry has an error outside the bounds reported for the experimental one, the objective function has been constructed such as to reproduce the latter. The results, including a discussion on the major topographical features of the SO_2 DMBE II potential energy surface so obtained are presented in Section 5. Moreover, a comparison with some of the most popular potential functions previously for the title system will then be also reported. Some concluding remarks are in Section 6.

2. Ab initio energies

The starting point to construct the DMBE II potential energy surface reported in this work is that reported elsewhere [27] from a fit to ab initio energies (582 points in all) calculated at the CASPT2 [38] (complete active space second-order perturbation theory) level using a FVCAS [39] (full valence complete active space) reference wave function [all calculations employed the aug-cc-pVTZ (AVTZ) basis set of Dunning [40,41], and have been carried out using the MOLPRO [42] package in C_s symmetry]. Suffice it to say here that the bulk of the calculated points refer to O–SO Jacobi coordinates defined by $2.506 \leq R_{SO}/a_0 \leq 3.306$, $2.0 \leq r_{O-SO}/a_0 \leq 6.0$, and $0 \leq \gamma \leq 180°$, with some extra energies being calculated for energies in the vicinity of the local minima and S–O_2 interactions (except when comparing with spectroscopic data where the energy will be expressed in cm^{-1}, atomic units will be employed throughout the paper); $\vec{R}_{SO}$ is the bond distance

SO vector pointing from the O to the S atoms, $\vec{r}_{O-SO}$ is the vector connecting the other O atom to the center of mass of the SO diatomic, and $\cos\gamma = (\vec{R}_{SO}\cdot\vec{r}_{O-SO}/|R_{SO}r_{O-SO}|)$. Due to convergence problems near the crossing of the two $^1A'$ surfaces, and the expected [38] loss of quality of the CASPT2 method in these regions, some calculated points close to the crossing seam have been discarded from the fitting procedure. Furthermore, to correct for the complete basis set limit and truncation of the CI expansion in the CASPT2 calculations, all calculated energies have been scaled using the DMBE-SEC [43] method.

3. The DMBE formalism: a brief survey

According to the DMBE [28] method, the single-valued SO_2 potential energy surface assumes the form

$$V(\mathbf{R}) = \sum_{i=1}^{3} V_i^{(2)}(R_i) + V_{EHF}^{(3)}(\mathbf{R}) + V_{dc}^{(3)}(\mathbf{R}) + V_{elec}^{(3)}(\mathbf{R}) \quad (1)$$

where $V_i^{(2)} = V_{EHF,i}^{(2)} + V_{dc,i}^{(2)}$; the upper index denotes as usual the rank of the n-body energy term, while the subscripts EHF, dc, and elec indicate the extended Hartree–Fock, dynamical correlation, and electrostatic components of the interaction energy. In turn, **R** denotes the set of all three bond distances. To represent the two-body energy terms, we have employed the EHFACE2U [44] (extended Hartree–Fock approximate correlation energy model with inclusion of the united-atom limit) model potential; for completeness, its form is summarized in Appendix A.

The three-body dynamical correlation energy has in turn been expressed as [45]

$$V_{dc}^{(3)} = \sum_{i=1}^{3}\sum_{n} f_i(\mathbf{R})\chi_n(r_i)C_n^{(i)}(R_i,\gamma_i)r_i^{-n} \quad (2)$$

where i labels the A–BC type channel associated with each atom–diatom interaction, $R_i \equiv R_{BC}$ is the diatomic internuclear distance, $r_i = r_{A-BC}$ is the separation of atom A from the center of mass of the diatomic BC, and γ_i is the angle formed by these two vectors. Furthermore, $C_n^{(i)}(R_i,\gamma_i)$ denotes the relevant atom–diatom long-range dispersion coefficient, $\chi_n(r_i)$ the associated dispersion damping function [46–48] (Appendix A), and $f_i(\mathbf{R})$ a switching function [45]. A convenient form for this is [45]

$$f_i = \frac{1}{2}\{1 - \tanh[\xi\eta s_i - s_j - s_k)]\} \quad (3)$$

where $s_i = R_i - R_{i,ref}$ with $R_{i,ref}$ being a convenient reference geometry; similar expressions apply to s_j and s_k, and to the other channels. For the coordinates, we have used the long-range approximations [27]

$$r_i = \frac{A_jR_j + A_kR_k}{A_j + A_k} \quad (4)$$

$$\cos\gamma_i = \frac{1}{2}\left[\frac{(R_k - R_j(R_k + R_j)}{R_i} + \frac{A_k - A_j}{A_k + A_j}R_i\right]/r_i \quad (5)$$

where A_i are parameters with values numerically equivalent to the atomic masses in SO_2. Note that such parameters are invariant to isotopic substitution, as the potential energy surface must be mass-independent in the Born–Oppenheimer sense. Note further that, for $A_i = A_j$, these expressions reduce to those reported elsewhere [28]. The atom–diatom dispersion coefficients assume their usual form [49]

$$C_n^{(i)}(R_i,\gamma_i) = \sum_L C_n^L(R_i)P_L(\cos\gamma_i) \quad (6)$$

where $P_L(\cos\gamma_i)$ are Legendre polynomials. As in Ref. [27], only the coefficients C_6^0, C_6^2, C_8^0, C_8^2,and C_{10}^0 have been used in the Legendre expansion of Eq. (6).

The three-body electrostatic energy in SO_2 has been approximated by

$$V_{elec}^{(3)} = \sum_{i=1}^{3} f_i(\mathbf{R})[C_4R_i,r_i)\mathscr{A}_{DQ}(\theta_{a,i},\gamma_i,\phi_{ab,i})r_i^{-4} + C_5(R_i,r_i)\mathscr{A}_{QQ}(\theta_{a,i},\gamma_i,\phi_{ab,i})r_i^{-5}] \quad (7)$$

where $f_i(\mathbf{R})$, R_i, r_i, and γ_i have the meaning assigned above, while $\theta_{a,i}$ is the angle that defines the atomic quadrupole orientation, and $\phi_{ab,i}$ is the corresponding dihedral angle. The coefficients $C_4(R_i,r_i)$ and $C_5(R_i,r_i)$ for the ith atom–diatom channel (for convenience, we include the associated damping functions) assume the form

$$C_4(R_i,r_i)=\frac{3}{2}\,Q_{\rm A}D_{\rm BC}(R_i)\chi_4(r_i)$$

$$C_5(R_i,r_i)=\frac{3}{4}\,Q_{\rm A}Q_{\rm BC}(R_i)\chi_5(r_i) \tag{8}$$

where $D_{\rm BC}(R_i)$ and $Q_{\rm BC}(R_i)$ are the electric permanent dipole and quadrupole moments of diatomic BC, respectively, and $Q_{\rm A}$ is the quadrupole moment of atom A. In turn, the angular variations of A_{DQ} and A_{QQ} are given by [50]

$$\begin{aligned}&\mathscr{A}_{DQ}(\theta_a,\gamma,\phi_{ab})\\&=\cos\gamma(3\cos^2\theta_a-1)\\&\quad+2\sin\theta_a\sin\gamma\cos\theta_a\cos\phi_{ab}\end{aligned} \tag{9}$$

$$\begin{aligned}&\mathscr{A}_{QQ}(\theta_a,\gamma,\phi_{ab})\\&=1-5\cos^2\theta_a-5\cos^2\gamma+17\cos^2\theta_a\cos^2\gamma\\&\quad+2\sin^2\theta_a\sin^2\gamma\cos^2\phi_{ab}\\&\quad+16\sin\theta_a\sin\gamma\cos\theta_a\cos\gamma\cos\phi_{ab}\end{aligned} \tag{10}$$

To eliminate the angle θ_a, [27], we have employed the classical-optimized-quadrupole (COQ) model [51–55] developed in our group. All coefficients in the above expressions assume the numerical values reported in Ref. [27] with the reader being referred to this work for details.

Thus, in the present work, only the coefficients of the three-body extended Hartree–Fock energy term need to be optimized to fit the experimental frequencies, the derivatives at the minimum, and the ab initio energy points. Following Ref. [27], $V^{(3)}_{\rm EHF}$ assumed the following distributed multinomial form [56]

$$\begin{aligned}V^{(3)}_{\rm EHF}=&P_\alpha(R_1,R_2,R_3)\prod_{i=1}^{3}\{1-\tanh[\gamma_i^\alpha(R_i-R_{i,\rm ref}^\alpha)]\}\\&+P_\beta(R_1,R_2,R_3)\\&\prod_{i=1}^{3}\{1-\tanh[\gamma_i^\beta(R_i-R_{i,\rm ref}^\alpha)]\}\end{aligned} \tag{11}$$

where

$$\begin{aligned}&P_\alpha(R_1,R_2,R_3)\\&=c_1+c_2Q_1+c_3Q_3+c_4Q_1^2+c_5S_{2a}^2+c_6Q_1Q_3\\&\quad+c_7S_{2b}^2+C_8Q_1^3+c_9Q_1S_{2a}^2+c_{10}S_3^3+c_{11}Q_1^2Q_3\\&\quad+c_{12}Q_1S_{2b}^2+c_{13}Q_3S_{2a}^2+c_{14}Q_1^4+c_{15}Q_1^2S_{2a}^2\\&\quad+c_{16}S_{2a}^4+c_{17}Q_1S_3^3+c_{18}Q_1^3Q_3+c_{19}Q_1^2S_{2b}^2\\&\quad+c_{20}Q_1Q_3S_{2a}^2+c_{21}Q_3S_3^3+c_{22}S_{2a}^2S_{2b}^2+c_{23}Q_1^5\\&\quad+c_{24}Q_1^3S_{2a}^2+c_{25}Q_1S_{2a}^4+c_{26}Q_1^2S_3^3+c_{27}S_{2a}^2S_3^3\\&\quad+c_{28}Q_1^4Q_3+c_{29}Q_1^3S_{2b}^2+c_{30}Q_1^2Q_3S_{2a}^2\\&\quad+c_{31}Q_1Q_3S_3^3+c_{32}Q_1S_{2a}^2S_{2b}^2+c_{33}Q_3S_{2a}^4\\&\quad+c_{34}S_{2b}^2S_3^3+c_{35}Q_1^6+c_{36}Q_1^4S_{2a}^2+c_{37}Q_1^22S_{2A}^4\\&\quad+c_{38}Q_1^3S_3^3+c_{39}Q_1S_{2a}^2S_3^3+c_{40}S_{2a}^6+c_{41}S_3^6\\&\quad+c_{42}Q_1^5Q_3+c_{43}Q_1^4S_{2b}^2\\&\quad+c_{44}Q_1^3Q_3S_{2a}^2+c_{45}Q_1^2Q_3S_3^3+c_{46}Q_1^2S_{2a}^2S_{2b}^2\\&\quad+c_{47}Q_1Q_3S_{2a}^4+c_{48}Q_1S_{2b}^2S_3^3+c_{49}Q_3S_{2a}^2S_3^3\\&\quad+c_{50}S_{2a}^4S_{2b}^2\end{aligned} \tag{12}$$

is a sixth-order polynomial in symmetry coordinates and $P_\beta(R_1,R_2,R_3)$ is a similar fifth-order polynomial with coefficients c_{51}–c_{84} (i.e. c_{51} will be the coefficient corresponding to c_1 in Eq. (12), and so on up to c_{84} which will correspond to c_{34}). As usual, the linear symmetry coordinates have been defined as [28,57]

$$\begin{bmatrix}Q_1\\Q_2\\Q_3\end{bmatrix}=\begin{bmatrix}\sqrt{1/3}&\sqrt{1/3}&\sqrt{1/3}\\\sqrt{1/2}&-\sqrt{1/2}&0\\-\sqrt{1/6}&-\sqrt{1/6}&\sqrt{2/3}\end{bmatrix}\begin{bmatrix}R_1\\R_2\\R_3\end{bmatrix} \tag{13}$$

with $S_{2a}^2+Q_2^2+Q_3^2$, $S_{2b}^2=Q_2^2-Q_3^2$, and $S_3^3=Q_3^3-3Q_2^2Q_3$. The complete set of parameters amounts to 84 linear coefficients c_i, four non-linear coefficients $\gamma_i^{\alpha,\beta}$, and four reference geometries $R_{i,\rm ref}^{\alpha,\beta}$. Their optimal numerical values are given in Table 4. Note that we have kept the non-linear parameters fixed at the optimum values obtained for DMBE I. In fact, no significant changes with respect to the values reported for DMBE I are expected since the spectroscopic data refers to regions of the potential energy surface where the range term in $V^{(3)}_{\rm EHF}$ should have little influence. Of course, a small tuning of such parameters can always be carried out for further improvement of the root mean-squared deviation (rmsd). However, being time consuming, such a strategy was not judged to be warranted prior to a test on

reaction dynamics studies of the potential energy surface so obtained, where such details may play a prominent role.

4. The least-squares fit: technical details

Our multiproperty least-squares fitting program uses the routine LMDER of the MINPACK [58] package, which is an improved version [59] of the Levenberg–Marquardt method. For the objective function, we have employed the form

$$F = \sum_{i=1}^{N} w_i \{V[\mathbf{R}(i)] - V_i^{ab}\}^2 + \sum_{v=1}^{M} w_v (E_v^{\mathrm{calc}} - E_v^{\mathrm{exp}})^2 + \sum_{i=1}^{L} \bar{w}_i \left\{\frac{\mathrm{d}V[\mathbf{R}(I)]}{\mathrm{d}R_i} - \frac{\mathrm{d}V_i}{\mathrm{d}R_i}\right\}^2 \quad (14)$$

which involves $N = 1474$ energy points V_i^{ab} (582 FVCAS/PT2 energies plus, as in Ref. [27], 855 long-range points generated with the sum of the two-body energies with the dispersion and electrostatic energies for $r_{\mathrm{O-SO}} > 7.0a_0$ and 32 short-range repulsive points generated using only the two body energies for diatomic bond distances $R_{\mathrm{AB}} < 1a_0$ to warrant the correct behavior at large and short distances respectively), $M = 125$ vibrational frequencies E_v^{exp}, and $L = 3$ first-derivatives of the potential at the global minimum ($\mathrm{d}V_i/\mathrm{d}R_i$). Thus, w_i, w_v, and $\bar{w}_i$ are the least-squares weights for the various sets of fitted data. For the ab initio energies, we have kept essentially identical to those used for DMBE I ($w_i = 1$ for points with E/E_{h}, $w = 10^3$ for 21 points around the three minima, and $w = 10^2$ for all the other points). In turn, the weights w_v are indicated for each individual vibrational frequency in Table 1, while the $\bar{w}_i$ ones are chosen sufficiently large ($\bar{w}_i = 10^4$) to reproduce the experimental equilibrium geometry of the open isomer within its reported error bounds.

The 125 fitted vibrational frequencies chosen to calibrate DMBE II consist of 31 observed experimental frequencies [3,4,6,10,60–66] and 84 values taken from the Dunham expansion of Yamanouchi et al. [8], covering a range of energies up to 6886 cm^{-1}. As noted in the previous paragraph, the weights employed on the global least-squares fit are indicated in column seven of Table 1 for all fitted vibrational levels, and have been assigned roughly according to the estimated uncertainties discussed in the literature [6,8,10]. An exception is the fundamental bending level, which carried an extra weight to improve the convergence of the least-squares fitting procedure.

At each step of the iterative fitting process (this involves typically 20 iterations or so) the lowest 150 vibrational levels (calculated for $J = 0$) of the potential energy function have then been calculated using Radau coordinates as implemented in the DVR3D program suite [67]. This employs a discrete variable representation (DVR) for each coordinate based on the approach of Tennyson and Sutcliffe [68]. For the radial coordinates, the number of the DVR grid points (based on Morse oscillator-like functions) have been set to 40 with the variational Morse parameters being optimized and set to $r_{\mathrm{e}} = 3.20a_0$, $D_{\mathrm{e}} = 0.19E_{\mathrm{h}}$, and $\omega_{\mathrm{e}} = 0.006E_{\mathrm{h}}$. For the bending coordinate, the number of grid DVR points (based on associated Legendre polynomials) have been set to 120. According to the DVR3D methodology [67], the calculation was then set up as a series of diagonalizations using the order $r_2 \rightarrow r_1 \rightarrow \theta$. An energy cut-off of -60000 cm^{-1} (the potential well of SO_2 DMBE II is -90670 cm^{-1}) has been employed for the calculation of the 1D states, and the maximum dimension of the 2D problems kept 1000 to obtain the final Hamiltonian matrix of dimension $N = 1500$. Based on comparisons with calculations employing larger Hamiltonian matrices and more functions per coordinate, the first 150 calculated vibrational levels up to about 7500 cm^{-1} are seen from the insert in Fig. 1 (the errors are obtained by subtracting the vibrational energies used in the present work employing the larger grid from those based on the smaller one) to be converged within 0.02 cm^{-1} or better. Moreover, Fig. 1 shows that the error remains smaller than 0.1 cm^{-1} for all calculated levels of relevance for the present work (Table 2).

Using the Hellmann–Feynman theorem, the derivatives of the energy levels with respect to the parameters of the potential energy surface have been calculated as expectation values of the potential derivatives [69]. Thus,

Table 1
Calculated vibrational energies (in cm^{-1}) for SO_2 and corresponding experimental values

(n_1,n_2,n_3)	Initial	Init.-exp.	Fit	Fit-exp.	Exp. [3,4,6–8,10,60–66]	$w_v/10^4$
(0 1 0)	513.5	−4.4	517.8	−0.1	517.9	100
(0 2 0)	1032.1	−3.0	1034.8	−0.3	1035.1	20
(1 0 0)	1197.1	45.4	1151.6	−0.2	1151.7	20
(0 0 1)	1282.4	−79.7	1362.0	−0.1	1362.1	20
(0 3 0)	1555.2	3.5	1551.3	−0.5	1551.7	10
(1 1 0)	1708.4	42.1	1667.0	0.6	1666.3	10
(0 1 1)	1791.9	−83.9	1875.2	−0.6	1875.8	10
(0 4 0)	2082.0	15.1	2067.2	0.4	2066.9	10
(1 2 0)	2224.5	44.2	2181.2	0.8	2180.3	10
(2 0 0)	2381.2	85.4	2294.7	−1.1	2295.8	10
(0 2 1)	2306.7	−82.2	2387.9	−1.0	2388.9	10
(1 0 1)	2466.5	−33.4	2499.4	−0.4	2499.9	10
(0 5 0)	2611.8	29.5	2582.7	0.4	2582.3	10
(1 3 0)	2744.7	51.1	2694.4	0.8	2693.6	10
(0 0 2)	2568.9	−144.5	2713.7	0.3	2713.4	10
(2 1 0)	2891.0	83.8	2807.9	0.8	2807.2	10
(1 1 1)	2973.8	−36.5	3010.3	0.0	3010.3	5
(0 6 0)	3144.1	48.5	3097.7	2.1	3095.6	1
(1 4 0)	3268.3	62.5	3206.8	1.0	3205.8	1
(0 1 2)	3074.3	−148.0	3222.4	0.1	3222.3	5
(2 2 0)	3405.1	87.0	3319.6	1.5	3318.1	1
(0 4 1)	3349.1	−63.9	3412.2	−0.8	3413.0	1
(3 0 0)	3554.0	122.8	3430.1	−1.1	3431.2	5
(1 2 1)	3486.1	−34.1	3520.3	0.1	3520.2	1
(0 7 0)	3678.3	69.4	3612.1	3.3	3608.9	1
(2 0 1)	3637.4	7.6	3628.3	−1.5	3629.8	5
(1 5 0)	3794.6	77.2	3718.3	1.0	3717.4	1
(0 2 2)	3585.2	−145.7	3730.8	−0.2	3730.9	5
(2 3 0)	3922.7	94.6	3829.8	1.8	3828.1	1
(1 0 2)	3739.0	−98.1	3836.7	−0.3	3837.1	5
(0 5 1)	3875.4	−48.4	3923.9	0.1	3923.8	1
(3 1 0)	4062.8	122.9	3941.4	1.5	3939.9	2
(1 3 1)	4002.6	−26.8	4029.5	0.1	4029.4	10
(0 0 3)	3857.9	−196.1	4054.9	0.9	4054.0	10
(0 8 0)	4214.0	92.7	4125.9	4.6	4121.3	1
(2 1 1)	4143.2	6.2	4137.1	0.2	4137.0	1
(1 6 0)	4323.2	95.1	4229.2	1.0	4228.1	1
(0 3 2)	4100.8	−140.7	4238.9	−2.6	4241.5	2
(2 4 0)	4443.4	100.7	4338.8	−3.9	4342.7	2
(1 1 2)	4242.3	−102.0	4343.3	−1.0	4344.3	1
(0 6 1)	4404.2	−29.7	4435.2	1.3	4433.9	1
(3 2 0)	4575.1	128.2	4450.7	3.8	4446.9	2
(1 4 1)	4522.5	−15.1	4538.0	0.4	4537.6	1
(4 0 0)	4716.9	156.8	4558.4	−1.7	4560.1	2
(0 1 3)	4359.2	−200.9	4559.1	−1.0	4560.1	1
(0 9 0)	4750.7	117.8	4638.9	5.9	4632.9	1
(2 2 1)	4653.4	9.9	4644.6	1.1	4643.5	1
(1 7 0)	4853.6	115.5	4739.2	1.1	4738.1	1
(0 4 2)	4620.2	−128.1	4746.9	−1.3	4748.3	1
(3 0 1)	4796.5	45.3	4749.2	−2.0	4751.2	2
(2 5 0)	4966.6	121.0	4846.8	1.2	4845.6	1
(1 2 2)	4750.8	−97.3	4849.1	0.9	4848.1	2

Table 1 (*Continued*)

(n_1,n_2,n_3)	Initial	Init.-exp.	Fit	Fit-exp.	Exp. [3,4,6–8,10,60–66]	$w_v/10^4$
(0 7 1)	4935.1	−8.2	4946.1	2.8	4943.3	1
(2 0 2)	4895.6	−58.2	4951.1	−2.8	4953.8	1
(3 3 0)	5090.6	135.5	4958.2	3.0	4955.1	1
(1 5 1)	5045.3	0.1	5045.9	0.7	5045.2	1
(0 2 3)	4866.1	−198.8	5063.2	−1.7	5064.9	1
(4 1 0)	5224.9	158.2	5068.0	1.3	5066.7	1
(2 3 1)	5167.3	18.0	5150.9	1.6	5149.3	1
(0 10 0)	5288.0	144.2	5150.9	7.1	5143.8	1
(1 0 3)	5013.1	−152.5	5163.4	−2.2	5165.6	1
(1 8 0)	5385.2	137.9	5248.3	1.0	5247.3	1
(0 5 2)	5142.9	−112.3	5254.8	−0.4	5255.2	1
(3 1 1)	5301.2	45.6	5256.3	0.6	5255.6	1
(2 6 0)	5491.8	138.7	5353.6	0.5	5353.1	1
(1 3 2)	5263.5	−91.4	5354.2	−0.6	5354.9	1
(0 0 4)	5148.2	−235.9	5385.5	1.3	5384.2	1
(2 1 2)	5397.5	−59.3	5455.7	−1.2	5456.8	1
(0 8 1)	5467.6	15.7	5456.4	4.5	5451.9	1
(3 4 0)	5608.6	147.5	5464.1	3.0	5461.1	1
(1 6 1)	5570.4	18.4	5553.1	1.1	5552.0	1
(0 3 3)	5377.9	−191.2	5567.2	−1.9	5569.1	1
(4 2 0)	5735.8	164.8	5575.1	4.0	5571.0	1
(2 4 1)	5684.3	29.9	5656.1	1.7	5654.4	1
(0 11 0)	5825.5	171.7	5661.8	8.0	5653.8	1
(1 1 3)	5512.4	−155.2	5665.6	−2.1	5667.6	1
(5 0 0)	5870.8	187.9	5680.0	−2.9	5682.9	1
(1 9 0)	5917.7	162.0	5756.5	0.8	5755.7	1
(3 2 1)	5809.7	50.7	5761.4	2.5	5759.0	1
(0 6 2)	5668.3	−93.1	5762.4	1.0	5761.4	1
(1 4 2)	5779.8	−79.3	5858.9	−0.2	5859.1	1
(2 7 0)	6018.5	158.6	5859.5	−0.4	5859.9	1
(4 0 1)	5945.2	79.6	5862.8	−2.8	5865.6	1
(0 1 4)	5645.2	−240.2	5885.2	−0.3	5885.4	1
(2 2 2)	5903.9	−55.3	5959.1	−0.1	5959.2	1
(0 9 1)	6001.1	41.3	5966.1	6.3	5959.8	1
(3 5 0)	6128.8	162.6	5968.5	2.3	5966.2	1
(3 0 2)	6040.4	−21.1	6057.3	−4.2	6061.5	1
(1 7 1)	6097.4	39.3	6059.7	1.6	6058.1	1
(0 4 3)	5893.6	−179.0	6071.2	−1.4	6072.6	1
(4 3 0)	6249.2	174.6	6079.9	5.3	6074.6	1
(2 5 1)	6203.9	45.2	6160.4	1.7	6158.7	1
(1 2 3)	6017.1	−152.1	6167.2	−1.9	6169.1	1
(0 12 0)	6362.6	199.7	6171.5	8.5	6162.9	1
(5 1 0)	6378.3	193.4	6188.0	3.1	6184.9	1
(2 0 3)	6154.8	−113.2	6263.0	−5.0	6268.0	1
(3 3 1)	6321.4	59.9	6265.0	3.5	6261.5	1
(1 10 0)	6450.7	187.5	6263.6	0.3	6263.2	1
(0 7 2)	6195.8	−71.0	6269.7	2.8	6266.8	1
(1 5 2)	6299.1	−63.6	6363.1	0.4	6362.7	1
(2 8 0)	6546.3	180.5	6364.2	−1.6	6365.8	1
(4 1 1)	6449.2	82.8	6368.1	1.7	6366.4	1
(0 2 4)	6148.1	−238.0	6384.9	−1.2	6386.1	1
(2 3 2)	6414.2	−46.7	6461.4	0.6	6460.9	1
(3 6 0)	6650.7	180.1	6471.6	1.1	6470.6	1
(0 10 1)	6535.3	68.4	6474.9	8.0	6466.9	1

Table 1 (*Continued*)

(n_1,n_2,n_3)	Initial	Init.-exp.	Fit	Fit-exp.	Exp. [3,4,6–8,10,60–66]	$w_v/10^4$
(1 0 4)	6287.8	−194.7	6479.2	−3.3	6482.5	1
(3 1 2)	6541.2	−20.0	6560.1	−1.1	6561.2	1
(1 8 1)	6625.7	62.3	6565.5	2.1	6563.4	1
(0 5 3)	6412.7	−162.8	6575.1	−0.4	6575.5	1
(4 4 0)	6764.8	187.4	6582.9	5.5	6577.4	1
(2 6 1)	6725.5	63.2	6663.8	1.5	6662.3	1
(1 3 3)	6526.1	−143.9	6668.4	−1.5	6670.0	1
(013 0)	6899.0	227.7	6679.6	8.3	6671.3	1
(5 2 0)	6887.9	201.8	6693.0	6.9	6686.1	1
(0 0 5)	6438.4	−264.0	6705.2	2.8	6702.4	1
(2 1 3)	6652.8	−114.0	6763.4	−3.4	6766.8	1
(3 4 1)	6835.7	72.4	6767.2	3.8	6763.3	1
(1 11 0)	6983.7	213.8	6769.4	−0.5	6769.9	1
(0 8 2)	6724.9	−46.7	6776.5	4.9	6771.6	1
(6 0 0)	7016.7	220.1	6795.4	−1.3	6796.6	1
(1 6 2)	6820.8	−44.7	6866.7	1.2	6865.5	1
(2 9 0)	7074.8	203.9	6867.8	−3.1	6870.9	1
(4 2 1)	6956.1	89.6	6871.2	4.7	6866.5	1
(0 3 4)	6655.9	−230.3	6884.7	−1.5	6886.2	1
rmsd		123.5		2.9		

$$\frac{\partial E_n}{\partial c_i} = \left\langle n \left| \frac{\partial V(R_1,R_2,R_3;c_i)}{\partial c_i} \right| n \right\rangle \tag{15}$$

using the wave functions calculated at the grid points. To identify the various vibrational levels, we have used the method of Menou and Leforestier [70]. According to their method, the vibrational quantum numbers for the title non-linear molecule are assigned automatically and calculated by using

$$n_i = \frac{1}{2}\left(\frac{\langle n|\Delta Q_i^2|n\rangle}{\langle 0|\Delta Q_i^2|0\rangle} - 1 \right) \tag{16}$$

where $\Delta Q_i^2 = Q_i^2 - \langle Q_i \rangle^2$, with Q_i denoting the ith normal mode eigenvector calculated at the equilibrium geometry. Such an automatic procedure has been of great help on the rather tedious but essential task of carrying out the assignment of the vibrational levels at each iterative step along the least-squares fitting procedure. Needless to say, such a task would be overwhelming if carried out non-automatically. However, care is required on such an assignment, especially if one departs from a potential function with a vibrational spectrum far different from the experimental one. Moreover, the highest overtone levels can become cumbersome to identify even through an eye-inspection, and hence an efficient assignment tool is essential for success in the implementation of the present least-squares approach. Even though the Menou–Leforestier [70] assignment scheme has been found useful for molecules as floppy as ground-state Li_3 [71], such an automatic method is in principle expected to be valid only for nearly harmonic spectra and well converged wave functions, and thus the quality of the assignment must be counterchecked and monitored. This has been done here by checking the assigned levels against the Dunham expansion

$$E_n = \sum_{i=1}^{3}\left(n_i+\frac{1}{2}\right)\omega_i + \sum_{i=1}^{3}\sum_{j=1}^{3}\left(n_i+\frac{1}{2}\right)\left(n_j+\frac{1}{2}\right)x_{ij} + \sum_{i=1}^{3}\sum_{j=i}^{3}\sum_{k=j}^{3}\left(n_i+\frac{1}{2}\right)\left(n_j+\frac{1}{2}\right)\left(n_k+\frac{1}{2}\right)x_{ijk} \tag{17}$$

and occasionally also through eye-inspection of sample wave function plots. Except for a few levels above the 150 working ones calculated for use in the least-squares fitting procedure of the present work (i.e. up to 7500 cm^{-1} or so), no assignment problems have been encountered. For higher energies, some incorrect assignments occurred, although part of the problems encoun-

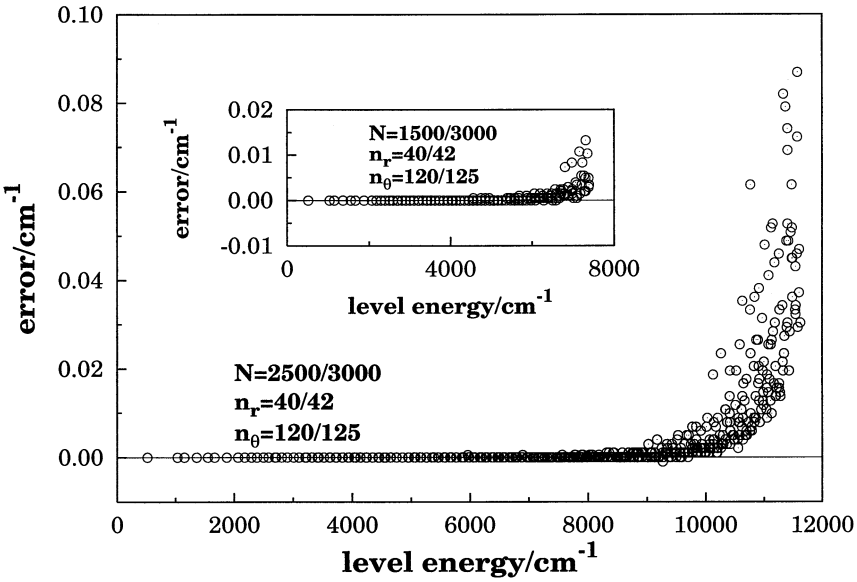

Fig. 1. Convergence test for the vibrational calculations carried out in the present work. The errors compare calculations based on different sizes of grids for the radial (N and n_r) and bending (n_θ) coordinates.

tered with those few high-energy levels could still be overcome by using an iterative procedure similar to that recommended in Ref. [70]. Basically, the procedure that we have used to assign automatically the 500 levels consisted of fitting the first 150 levels assigned to a Dunham expansion, which was then used to check and/or eventually reassign the higher levels. Specifically, if for the same quantum numbers the difference between the calculated and Dunham predicted energies for a given level was less than a threshold of 20 cm^{-1} or if the quantum numbers differed by a maximum of an unity each (with the difference in energy between the calculated level and that predicted from the Dunham expansion being less than the above threshold), the Dunham quantum numbers were accepted and the level would go to the group of the assigned ones. Once all levels have been considered, the Dunham expansion has been recalculated to check the quality of the assignment. In this way (i.e. after one iteration) only eight of the original 500 levels could not be properly assigned. Those failing to satisfy the above criteria correspond to high bending levels. Perhaps, they could all have been assigned by continuing the iterative process, although this was not deemed necessary in the present work.

For illustrative purposes, we show in Fig. 2 sample vibrational wave functions corresponding to the (2 3 2) and (3 8 2) levels. As seen from their nodal structures, the assignment has been correctly done through the above automatic procedure. It should be noted at this stage that an equivalent automatic procedure based on a perturbational approach has been suggested by Ma and Guo [12]. Although their method is especially valuable when the wave function is not explicitly calculated, it may turn out to be computationally more demanding, and hence it has not been used here. We should also emphasize that we have started the least-squares

Table 2
Stratified root mean squared deviations between the calculated SO_2 DMBE potential energy surface and ab initio energies

Number of points	Energy (kcal mol^{-1})	rmsd (kcal mol^{-1})
25	20	0.92
57	40	1.13
89	60	1.69
118	80	3.00
157	100	3.11
240	120	2.97
1365	200	2.25

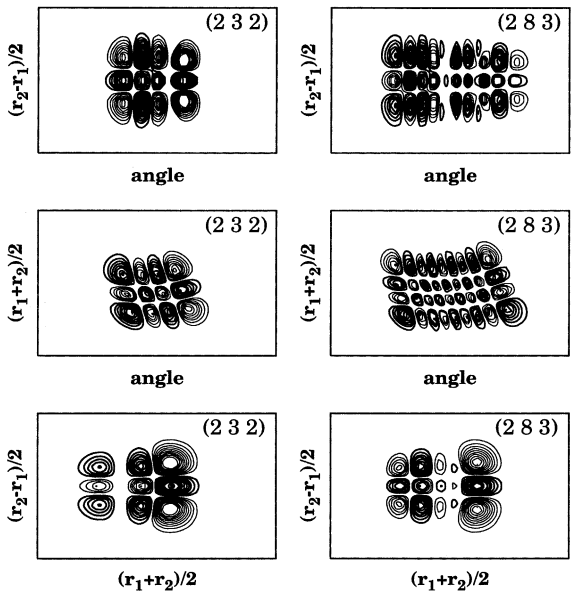

Fig. 2. Contour plots of the vibrational wave functions for the levels (2 3 2) and (3 8 2) with energies 6451.4 and 10042.3 cm^{-1}, respectively. Shown by the solid dark lines are the positive contours, while the thin lines indicate negative contours. Clearly, the nodal structure corroborates the assignment made using the automatic Menou–Leforestier [68] procedure employed in the present work.

fitting procedure using the set of parameters reported in Ref. [27] for the coefficients in Eq. (11). The calculated deviations at the initial and final iterative steps are reported in Table 1. Clearly, significant improvements are observed along the least-squares fitting procedure. For example, while the maximum deviation observed originally for the (0 0 5) level reaches -264 cm^{-1}, such a discrepancy has been reduced to only -2.8 cm^{-1} after convergence has been reached (this was achieved after 28 iterations). A significant improvement is also observed for the rmsd: it was originally 123.5 cm^{-1}, a value which was reduced to only 2.9 cm^{-1} for the final SO_2 DMBE II potential energy surface. Fig. 3 shows a scatter plot of the differences between the calculated and experimental vibrational energies as a function of the energy measured with respect to the zero-point energy of the equilibrium SO_2 potential well. Also shown in the insert of this figure are the errors found for the progressions $(n_1\,0\,0)$, $(0\,n_2\,0)$, and $(0\,0\,n_3)$. Clearly, the largest error after convergence is 8.5 cm^{-1}, which is observed for the (0 12 0) level. Indeed, as already noted above, bending overtones and their combinations with other modes tend to display the largest deviations (at least up to 7500 cm^{-1} or so), a fact already noted by Zúñiga et al. [14]. This led these authors to make a detailed selection of the input data prior to the fitting procedure. Rather then following their approach, we have chosen to test the robustness of our multiproperty fitting technique by including all levels up to about 6900 cm^{-1}, in a total of 125. Thus, besides truly observed levels, we have included some levels determined from the Dunham-type expansion derived by Yamanouchi et al. [8]. In fact, an extra least-squares fit has been carried out which employed as input data only the vibrational levels pre-selected by Zúñiga et al. [14] for their own fit. Since these results add little to those based on the 125 levels, we concentrate only on the latter (DMBE II) in the remaining of this paper.

5. Results and discussion

Table 3 reports all identified stationary points on the final SO_2 DMBE II potential energy surface. Following Ref. [27], these have been found by using a Newton–Raphson type method in which the starting guess point was chosen randomly. A total of 2×10^4 trials in Cartesian coordinates has been employed. Clearly, the geometry, energy and harmonic frequencies of the global minimum (which is the open SO_2 isomer) are well known experimentally, and are shown to be well reproduced by the final DMBE II potential energy surface. The ring (denoted r-SO_2 in the Table 3) and superoxide isomers have only been studied using ab initio methods. The agreement with the latter is fairly good, and even somewhat improved in relation to DMBE I when judged from the energetics point of view (see Table 2). The same comment applies to the transition state TS7, which is seen to be in good agreement with the prediction of the Morse-cosine expansion by Zúñiga et al. [14]. In fact, their saddle point for linear OSO structures underestimates TS7 in DMBE II by only 0.5 kcal mol^{-1}. All other topographical features reported in Table 3 afford

a comparison only with those reported for the SO_2 DMBE I potential energy surface. For simplicity, these have not been included in Table 3, since the two SO_2 DMBE functions are rather similar topographically. In fact, the only novel feature of DMBE II which is not observed in DMBE I is the appearance of a further transition state (TS6). This results from the splitting of TS4 (in DMBE I) into two transition states in DMBE II (TS4 and TS6) which have a very small maximum (the height of this is only a few tenths of a mE_h, i.e. less than 0.1 kcal mol^{-1}) separating them.

Fig. 4 shows the C_{2v} bending potential of the SO_2 DMBE II potential energy surface with the SO bond distances optimized at each value of the valence angle. Also included for comparison, are the corresponding curves referring to the many-body expansion potential of Carter et al. [31], and the DMBE I potential energy surface reported by the authors and Sabín [27]. Moreover, we have included the optimum bending curves for the Morse-cosine potential expansion of Zúñiga et al. [14]. In addition, we indicate by the horizontal line segments the calculated energy levels based on the SO_2 DMBE II potential energy surface from the present work. Perhaps, the most important feature to note comes from the comparison of the DMBE I and DMBE II SO_2 optimized bending curves. Although small, significant deviations are observed nearly at the bottom of the well. Such deviations are perhaps less important when one moves to high energies above the potential barrier for linearization. The other relevant feature concerns the shape of the reported curves. Although showing significant deviations both for angles smaller and larger than the equilibrium value, it is interesting to note that the Carter et al. [31] many-body expansion curve has a shape similar to the DMBE II one, especially having in mind that only force field information referring to the stable SO_2 C_{2v} species has essentially been used to calibrate the former. Addressing now the Dunham expansion, we observe strong deviations for levels above 10^4 cm^{-1} or so. This may suggest that such type of expansions should perhaps be viewed with caution when used to fit highly excited vibrational levels no matter how good the final fit can be. In fact, strong anharmonicities will be present, and one wonders if a good fit of the vibrational energies may mean more than that when referring to the assignment of

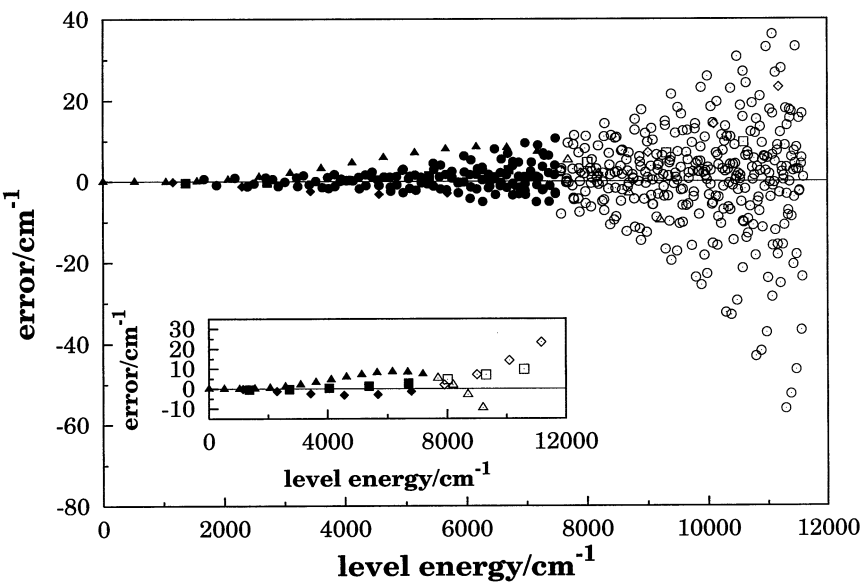

Fig. 3. Scatter plot of the errors between the calculated and experimental vibrational energy levels as a function of energy. Shown by the solid circles are the fitted levels, while the non-fitted ones are indicated by the open circles. The insert shows the errors obtained for the various progressions. These are indicated with different symbols: (n_1 0 0), squares; (0 n_2 0), triangles; (0 0 n_3), diamonds. The overtone combinations are indicated with circles.

Table 3
Stationary points of the SO_2 DMBE potential energy surface. Harmonic frequencies are in cm^{-1}, and ΔE in kcal mol^{-1}. Available experimental and theoretical data are given in parentheses

Feature	R_1/a_0	R_2/a_0	R_3/a_0	∠OSO (°)	E/E_h	ΔE	ω_1	ω_2	ω_3
SO_2	2.704	2.704	4.667	119.3	−0.4132	259.3[a]	1169	522	1381
	(2.704)[b]	(2.704)[b]	(4.667)[b]	(119.3)[b]		(259.3)[c]	(1168)[d]	(522)[d]	(1382)[d]
r-SO_2	3.189	3.189	2.758	51.2	−0.2402	108.6[e]	881	1039	874
	(3.194)[f]	(3.194)[f]	(2.835)[f]	(52.8)[f]		(104.0)[f]	(739)[f]	(1088)[f]	(805)[f]
SOO	3.089	4.723	2.460	27.9	−0.2299	115.0[e]	1075	619	591
	(3.079)[f]	(4.821)[f]	(2.483)[f]	(26.5)[f]		(112.8)[f]	(1384)[f]	(525)[f]	(929)[f]
O···OS	2.804	6.658	4.776	38.1	−0.2159	−10.6[g]	1055	118	289
S···O_2	4.620	4.620	2.178	27.3	−0.2236	−20.1[h]	450	1836	139
TS1	3.915	4.842	2.225	26.9	−0.2221	−19.2[h]	1665	524	222*i*
TS2	3.115	3.977	2.659	41.9	−0.1937	−1.3[h]	1156	747*i*	673
TS3	3.174	3.174	3.247	61.5	−0.2275	−22.5[h]	1000	830*i*	735
TS4	2.832	5.109	4.815	67.8	−0.2025	−2.2[g]	1001	170	310*i*
TS5	2.840	5.230	3.409	36.8	−0.2044	−3.4[g]	1041	393	472*i*
TS6	2.820	6.178	5.919	71.4	−0.2026	−2.2[g]	1073	240*i*	91
TS7	2.758	2.758	5.517	180	−0.3310	51.6[e]	872	531*i*	1477
	(2.731)[i]	(2.731)[i]	(5.462)[i]	(180)[i]		(52.1)[i]			

[a] Atomization energy.
[b] Experimental geometry [83].
[c] Experimental atomization energy; see Ref. [25].
[d] Experimental harmonic frequencies from Ref. [10].
[e] Energy referred to the open SO_2 isomer.
[f] Ab initio results with the energy referred to the open SO_2 isomer [24].
[g] Energy referred to the channel O+SO (−0.1990 E_h).
[h] Energy referred to the channel S+O_2 (−0.1916 E_h)
[i] Ref. [14]; energy referred to the open SO_2 isomer.

the vibrational levels. A final comment goes to the Morse-cosine potential expansion of Zúñiga et al. [14]. If one ignores angles shorter than about 80° where the potential extrapolates erroneously, it is significant to observe that it performs well in predicting the barrier for C_{2v} linearization of SO_2.

Perhaps a more suggestive illustration of the topography of the SO_2 DMBE II potential energy surface can be seen from Figs. 5 and 6. The former shows a contour plot for an oxygen atom moving around a SO diatomic, whose center of mass is kept fixed at the origin, while Fig. 6 shows a similar plot but for S moving around O_2. Also shown in Fig. 5 by the solid dots are the ab initio energies used in the multiproperty least-squares fitting procedure. Note that rays of points have been calculated points for several values of the SO bond distance, although only one such set is visible in the plot of Fig. 5 as the points for the various rays overlap each other. Also visible from this plot are the minima associated to various structures. On the left is the minimum corresponding to the open SO_2 molecule, while on the right (from bottom to top) are the minima associated to the superoxide and SO···O structures. In turn, for $x \sim 1a_0$ and $y \sim 2.5a_0$, is the minimum associated to the ring SO_2 species. Visible in Fig. 6 are the two symmetrical minima corresponding to the superoxide structure, and for $x = 0$ the ring SO_2 one. Just above this minimum one finds a maximum which is perhaps an artifact of the representation as it may correspond to a crossing of an excited repulsive potential energy surface with the 2^1A_1 one at C_{2v} geometries. Note that the 2^1A_1 surface (which contains the ring-SO_2 structure) shows a further, well established [15,23] crossing with the $\tilde{X}^1A_1$ potential energy surface at shorter distances. Of course, all become of A' symmetry for C_s geometries (i.e. the ring-SO_2 species will appear in the lowest A' surface). To our knowledge, no ab initio calculations have been carried out thus far

close to the intersection of the repulsive $^1A'$ surface with $2^1A'$ occurs, which might help to clarify this issue. This will hopefully be addressed in future work. Also visible from both Figs. 5 and 6 the fact that both the $S + O_2 \rightarrow SO + O$ reaction is predicted to occur without an energy barrier, at least along favorable directions for the atom attacking the diatomic. Moreover, Figs. 5 and 6 allow also a direct comparison with those reported elsewhere [27] for DMBE I, from which it is seen that only small topographical alterations resulted from the inclusion of vibrational levels into the fitting procedure. Perhaps, the most salient difference refers to the plot in Fig. 6 which shows a slightly narrower entrance channel for insertion of the S atom into O_2, and hence may have consequences on the dynamics of the reaction $S + O_2 \rightarrow SO + O$. However, since this narrowing is accompanied in DMBE II by a more pronounced decrease in energy when leading to the $S\cdots O_2$ structure (see Fig. 7), it is difficult to say a priori how such changes influence the dynamics attributes. Note that very few ab initio points have been calculated in this region, as it lies close to the crossing seam where difficulties are expected with the FVCAS/PT2 method. In general terms, we may then say that the DMBE I and DMBE II potential energy surfaces show generally similar topographies, which supports the good quality of the DMBE I [27] starting function. It also gives credit to the accuracy of the FVCAS/PT2 points [27] on which the latter has been based upon. Furthermore, it supports the observation [14,72] that the coefficients obtained from a fit to reliable ab initio data may offer the ideal starting point for any fitting strategy aiming at potential energy surfaces with spectroscopic accuracy.

A further comparison of the various potentials reported for the title system is provided in the 1D plot of Fig. 8. It shows the variation of the potential energy along the OS–O dissociation coordinate (ρ) for the process $SO_2 \rightarrow SO + O$; the $\angle$OSO valence angle has been kept fixed at its equilibrium value of 119.3° while the unbroken SO bond distance has been optimized at each ρ value. The notable feature, though not unexpected, is the fact that both the Kauppi and Halonen [34] and the Morse-cosine expansion of Zúñiga et al. [14] dissociate incor-

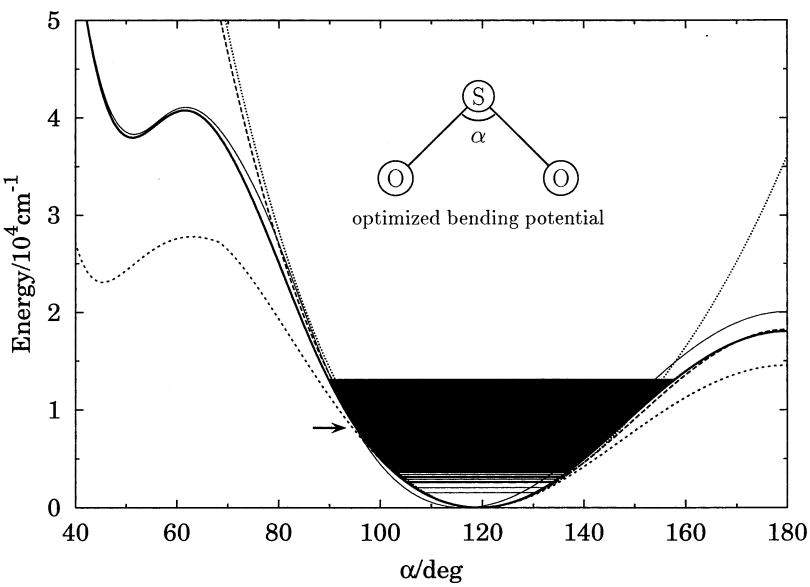

Fig. 4. The bending potential of SO_2, maintaining C_{2v} symmetry, for optimum values of the S–O bond lengths. The solid dark line indicates the DMBE II potential energy surface from the present work, while DMBE I [27] is indicated by the solid thin line. Also shown are the curves for the Carter et al. [31] many-body expansion potential energy surface (small-dash line), and for the Kauppi–Halonen [34] (dotted line) and Morse-cosine [14] (long-dash line) expansions. The horizontal line segments show the calculated vibrational level for DMBE II, while the arrow indicates the highest energy level considered for the fitting procedure.

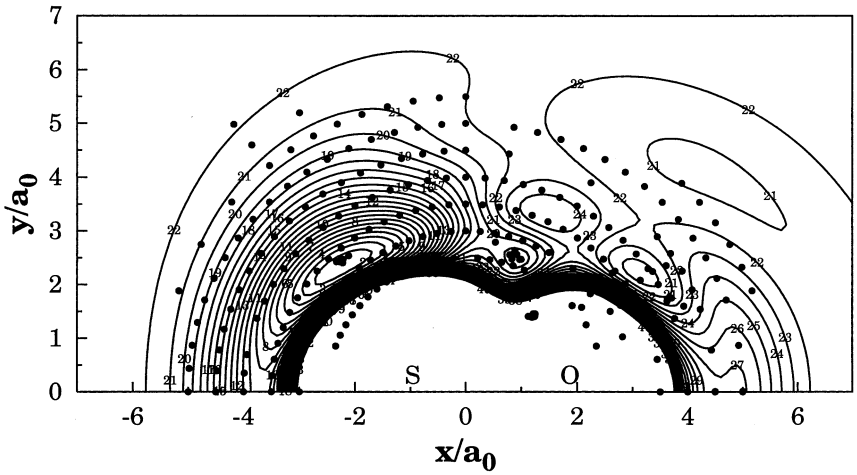

Fig. 5. Contour plot of DMBE II potential energy surface for an oxygen atom moving around a partially relaxed SO molecule ($2.6988 \leq R_{SO}/a_0 \leq 3.2289$) whose center of mass is kept at the origin. Contours start at $E_{min} = -0.4141\ E_h$, and are equally spaced by $\Delta E = 0.01\ E_h$. Shown by the solid dots are the calculated ab initio energies.

rectly, with the latter describing somewhat better the dissociation curve at the asymptotic limit. Significant differences are also observed over the region $3.2 \leq \rho/a_0 \leq 4.7$ between the Carter et al. [31] many-body expansion and DMBE II curves, although they both dissociate correctly. In turn, except at intermediates values of ρ ($\sim 5a_0$) the SO_2 DMBE I curve is seen to agree nicely with DMBE II, as implied from the discussion above.

Panels (a) to (c) of Fig. 9 show the minimum energy paths (in the steepest descent sense) that connect the various saddle-points and minima in the SO_2 DMBE II potential energy surface. As usual, the asymptotic regions of these plots have been calculated by starting with the atom far away from the diatomic. For the $S + O_2$ channel, all angles where the potential is attractive lead to the TS1 saddle-point. For the $O + SO$ channel two possibilities can occur: for angles where the oxygen atom moves toward the sulfur atom (i.e. for $O + SO$ configurations) the path goes directly to the global minimum. Instead, when the oxygen atom faces the other oxygen atom (i.e. for $O + OS$ configurations), the path goes through the SO···O minimum. The connection between the other minima and the saddle-points can also be seen on these plots, except for the saddle-point TS7 which occurs for linear geometries with $D_{\infty h}$ symmetry. Clearly, a comparison of these plots with those reported elsewhere [27] for the SO_2 DMBE I potential energy surface show only small differences. The most visible is perhaps that referring to the S···O_2 van der Waals well, which in DMBE II lies closer in energy to the superoxide SOO structure. In both cases though, the S···O_2 and SOO minima are separated from each other by only a small energy barrier (TS1).

6. Concluding remarks

We have been showing over the years [28,29] that the DMBE method can provide a reliable tool for representing the potential energy surfaces of polyatomic molecules over the entire molecular configurational space. In this paper, the method has been used for the first time to construct a single-valued function for SO_2 which reaches near spectroscopic accuracy at regions in the vicinity of the equilibrium molecular geometry while fitting simultaneously a large number of correlated ab initio energies covering an energy range of more than 200 kcal mol^{-1}. For this, we have used our recently proposed distributed n-body polynomial approach to express the extended Hartree–Fock part of the molecular energy, with the coefficients appearing in each polynomial being determined from a multiproperty fit to accurate DMBE-SEC

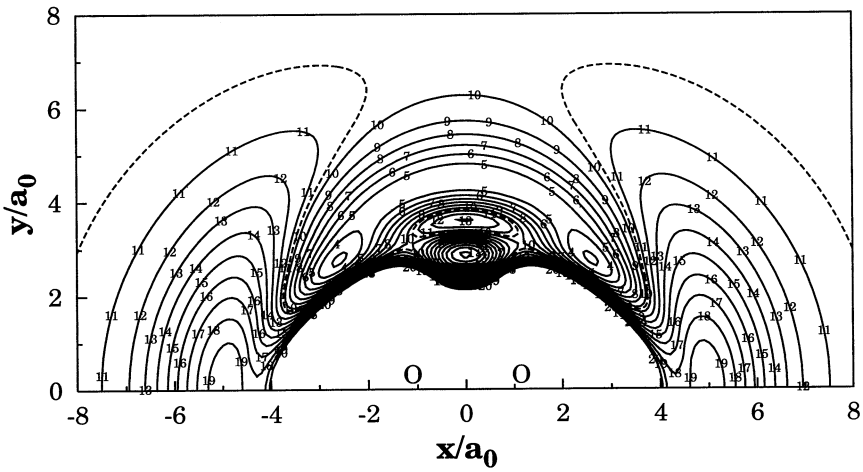

Fig. 6. Contour plot of DMBE II potential energy surface for a sulfur atom moving around a partially relaxed O_2 molecule ($2.1838 \leq R_{SO}/a_0 \leq 2.9839$) whose center of mass is kept fixed at the origin. Contours start at $E_{min} = -0.2389\ E_h$ and $\Delta E = 0.005\ E_h$. The dashed line represents the energy of dissociation to $S + O_2$.

energies and vibrational energy levels (Table 4). These have been calculated along the iterative least-squares procedure by using the DVR3D program suite as a system call derived by the master least-squares fitting code. Clearly, since we have adopted a single-valued formalism for the representation, no attempt was made to accurately model important topological features such as those associated with crossing seams of electronic states of the same symmetry and spin multiplicity. However, the reported single-valued DMBE II potential energy surface should be reliable for regions away from such a seam, and often even relatively close to it. A more careful examination of this issue will hopefully be done in future work. Thus, although it has recently become clear that interpolating techniques [73,74] of various sorts can offer a reliable route to construct semi-numerical type potential energy surfaces for small polyatomic systems from accurate ab initio data, it remains to be shown how such approaches can be used in multiproperty fits such as the one described in the present work. Indeed, besides providing the potential energy surface in a compact physically motivated form, the present approach can readily be extended for larger polyatomic systems (Ref. [75], and references therein) for which such interpolation techniques can hardly be expected to be computationally affordable. A final comment concerns the energy-switching (ES) method developed by one of us [45], which has since been successfully used to construct global functions with spectroscopic accuracy for various triatomic [45,76–78] and tetratomic [79] systems. One may argue that such an ES scheme may have the advantage of achieving the goal aimed at in the present work at perhaps a

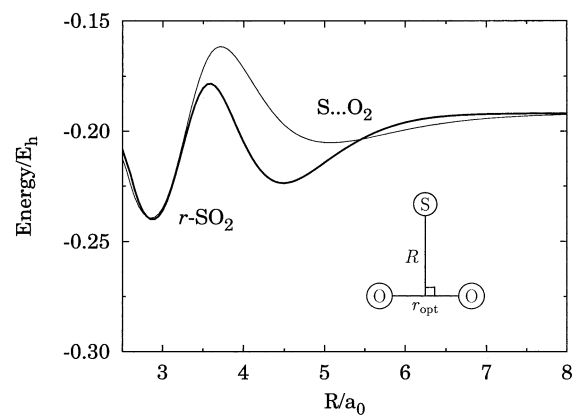

Fig. 7. Optimized potential curve for C_{2v} approach of an S atom to O_2: dashed line, DMBE I; solid line, DMBE II. For each value of the atom–diatom separation the O_2 bond distance is allowed to relax as in Fig. 6 such as to minimize the energy. The r-SO_2 and S···O_2 structures are also indicated. Having in mind that the 'maximum' separating them should rather be a crossing, it becomes apparent that such species lie on different adiabatic potential energy surfaces of the same symmetry.

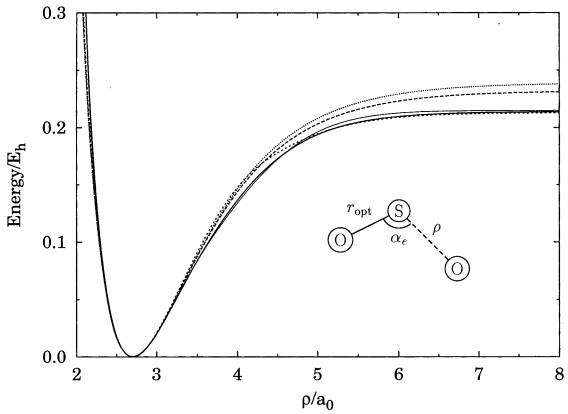

Fig. 8. Potential energy alone the OS–O dislocation coordinate for the process $SO_2 \rightarrow SO + O$; the $\angle OSO$ valence angle has been kept fixed at its equilibrium value of 119.3° while the unbroken SO bond distance is optimized at each value of the OS–O dissociating coordinate. Key for lines as in Fig. 4.

much lower cost. Indeed, it is even fair to say that the ES method may generally be more efficient since different forms and sets of coefficients are used to construct different parts of the potential energy surface at distinct energy regimes, which are then merged together to achieve a global analytic form. Of course, the DMBE II potential energy surface reported in the current work has the merit of compactness, since it uses the same physically motivated formalism to represent the whole potential energy surface. Thus, it will be interesting to compare how an ES potential energy surface for the title molecule performs when compared with DMBE II, especially in studying the dynamics of the reaction $S + O_2 \rightarrow SO + O$ reaction.

Acknowledgements

This work has the support of Fundação para a Ciência e Tecnologia under the PRAXIS XXI and SAPIENS programs.

Appendix A. The EHFACE2U model for diatomics

The EHFACE2U model assumes the general form [44,80] $V = V_{EHF} + V_{dc}$, where

$$V_{dc} = -\sum_{n=6,8,10} C_n \chi_n(R) R^{-n} \quad \text{(A1)}$$

and the damping dispersion functions are written as [46–48]

$$\chi_n(R) = \left[1 - \exp\left(-A_n \frac{R}{\rho} - B_n \frac{R^2}{\rho^2}\right)\right]^n \quad \text{(A2)}$$

with A_n and B_n being the auxiliary functions [47] $A_n = \alpha_0 n^{-\alpha_1}$ and $B_n = \beta_0 \exp(-\beta_1 n)$; $\alpha_0 = 16.36606$, $\alpha_1 = 0.70172$, $\beta_0 = 17.19338$, and $\beta_1 = 0.09574$ are universal parameters (dimensionless) for all isotropic interactions. In turn, the scaling parameter is defined by $\rho = (5.5 + 1.25R_0)$, where $R_0 = 2(\langle r_X^2 \rangle^{1/2} + \langle r_Y^2 \rangle^{1/2})$ with $\langle r_X^2 \rangle (\langle r_Y^2 \rangle)$ being the expectation value of the squared radii for the outermost electrons in atom X(Y) [81].

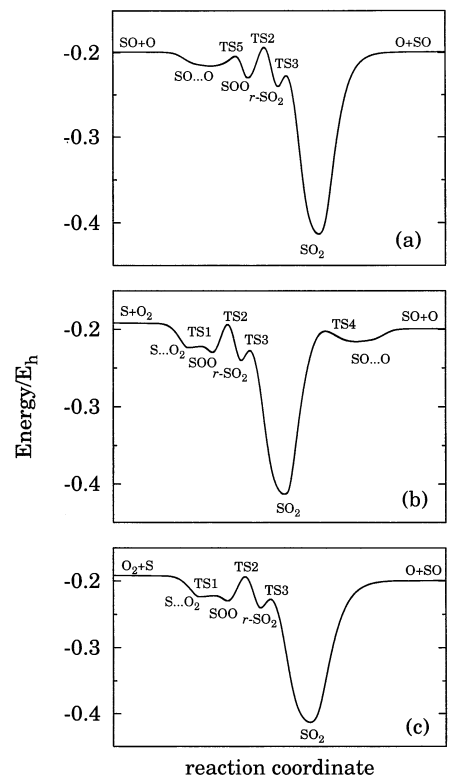

Fig. 9. Minimum energy paths connecting the most significant stationary points of the DMBE II potential energy surface and the various dissociation channels.

Table 4
Numerical values of the extended Hartree–Fock energy (Eq. (11)) in atomic units

$\gamma_1^{\alpha}=\gamma_2^{\alpha}=0.69$	$\gamma_2^{\alpha}=0.75$	
$\gamma_1^{\beta}=\gamma_2^{\beta}=1.35$	$\gamma_2^{\beta}=1.00$	
$R_{1,\mathrm{ref}}^{\alpha}=R_{2,\mathrm{ref}}^{\alpha}=2.7$	$R_{1,\mathrm{ref}}^{\alpha}=4.6$	
$R_{1,\mathrm{ref}}^{\beta}=R_{2,\mathrm{ref}}^{\beta}=3.1$	$R_{1,\mathrm{ref}}^{\beta}=2.8$	
$C_1=-250.27731763$	$C_2=273.68290084$	$C_3=-149.66418978$
$C_4=-127.72186396$	$C_5=22.26082986$	$C_6=133.62249462$
$C_7=23.68214853$	$C_8=32.20511930$	$C_9=-14.46158221$
$C_{10}=-1.54865790$	$C_{11}=-48.16647238$	$C_{12}=-16.30599007$
$C_{13}=-1.38649237$	$C_{14}=-4.58829205$	$C_{15}=3.51672485$
$C_{16}=0.78625232$	$C_{17}=0.86477531$	$C_{18}=8.74340065$
$C_{19}=4.22563726$	$C_{20}=-0.86037233$	$C_{21}=0.52159989$
$C_{22}=-1.75162940$	$C_{23}=0.34864013$	$C_{24}=-0.37801980$
$C_{25}=-0.26799825$	$C_{26}=-0.15168344$	$C_{27}=0.00443123$
$C_{28}=-0.80000778$	$C_{29}=-0.49247797$	$C_{30}=0.34768133$
$C_{31}=-0.14847560$	$C_{32}=0.55651304$	$C_{33}=0.07858827$
$C_{34}=0.08351093$	$C_{35}=-0.01100878$	$C_{36}=0.01514881$
$C_{37}=0.02104020$	$C_{38}=0.00832060$	$C_{39}=0.00475602$
$C_{40}=0.01288784$	$C_{41}=0.00042789$	$C_{42}=0.02944578$
$C_{43}=0.02158879$	$C_{44}=-0.02724018$	$C_{45}=0.01093405$
$C_{46}=-0.04028152$	$C_{47}=-0.01956493$	$C_{48}=-0.01485497$
$C_{49}=-0.01982732$	$C_{50}=-0.02221950$	$C_{51}=221.56795057$
$C_{52}=-236.89044091$	$C_{53}=137.30197251$	$C_{54}=103.98462384$
$C_{55}=-16.41409970$	$C_{56}=-114.63489734$	$C_{57}=-23.93658338$
$C_{58}=-23.23778521$	$C_{59}=9.97100685$	$C_{60}=3.25411113$
$C_{61}=36.65136398$	$C_{62}=14.34751974$	$C_{63}=1.45833493$
$C_{64}=2.63006006$	$C_{65}=-1.97058231$	$C_{66}=1.01268997$
$C_{67}=-1.19016602$	$C_{68}=-5.29094332$	$C_{69}=-2.92056020$
$C_{70}=-0.15293764$	$C_{71}=0.86214940$	$C_{72}=1.01557894$
$C_{73}=-0.12034889$	$C_{74}=0.12577867$	$C_{75}=-0.12833028$
$C_{76}=0.10378730$	$C_{77}=-0.15310871$	$C_{78}=0.29022464$
$C_{79}=0.20263507$	$C_{80}=-0.01610854$	$C_{81}=-0.16566627$
$C_{82}=-0.17586035$	$C_{83}=0.45925352$	$C_{84}=-0.07104151$

In turn, the V_{EHF} component of the potential is written as [44]

$$V_{\mathrm{EHF}}=-DR^{-1}\left(1+\sum_{i=1}^{N}a_i r^i\right)\exp[-\gamma(r)r]+V_{\mathrm{exc}}^{\mathrm{asym}}(R)\chi_{\mathrm{exc}}(R) \quad \text{(A3)}$$

where $\gamma(r)=\gamma_0[1+\gamma_1\tanh(\gamma_2 r)]$, $r=R-R_m$ is the displacement from the equilibrium geometry, and D, $a_i(i=1-N)$ and γ_i $(i=0\text{–}2)$ are parameters usually determined from a least-squares fitting procedure to RKR and/or other available data. Moreover, $V_{\mathrm{exc}}^{\mathrm{asym}}$ is the asymptotic exchange energy. For the numerical coefficients of relevance in the present work, see Refs. [27,56,82].

References

[1] B.J. Finlayson-Pitts, J.N. Pitts Jr., Atmospheric Chemistry, Wiley, New York, 1986.
[2] K. Schofield, Combust. Flame 124 (2001) 137.
[3] R.D. Shelton, A.H. Nielsen, W.H. Fletcher, J. Chem. Phys. 2178 (1953) 21.
[4] J.C.D. Brad, D.R. Humphrey, A.E. Douglas, I. Zanon, Can. J. Phys. 51 (1973) 530.
[5] G. Guelachvili, O. Naumenko, O. Ulenikov, J. Mol. Spectrosc. 124 (1987) 128.
[6] L. Coudert, A.G. Maki, W.B. Olson, J. Mol. Spectrosc. 124 (1987) 437.
[7] K. Yamanouchi, H. Yamada, S. Tsuchiya, J. Chem. Phys. 88 (1988) 4664.
[8] K. Yamanouchi, S. Takeuchi, S. Tsuchiya, J. Chem. Phys. 92 (1990) 4044.

[9] W.J. Lafferty, G.T. Fraser, A.S. Pine, J.-M. Flaud, C. Cammy-Peyret, V. Dana, J. Mandin, A. Barbe, J.J. Plateaux, S. Bouazza, J. Mol. Spectrosc. 154 (1992) 51.
[10] W.J. Lafferty, A.S. Pine, J.-M. Flaud, C. Cammy-Peyret, J. Mol. Spectrosc. 157 (1993) 499.
[11] G. Ma, H. Guo, J. Chem. Phys. 110 (1999) 8408.
[12] G. Ma, H. Guo, J. Chem. Phys. 111 (1999) 4032.
[13] D. Xie, H. Guo, O. Bludský, P. Nachtigall, Chem. Phys. Lett. 329 (2000) 503.
[14] J. Zúñiga, A. Bastida, A. Requena, J. Chem. Phys. 115 (2001) 139.
[15] H. Katagiri, T. Sako, A. Hishikawa, T. Yazaki, K. Onda, K. Yamanouchi, K. Yoshino, J. Mol. Struct. 413 (1997) 589.
[16] P.C. Ray, M.F. Arendt, L.F. Butler, J. Chem. Phys. 109 (1998) 5221.
[17] S.C. Farantos, J.N. Murrell, Chem. Phys. 55 (1981) 205.
[18] J.H. Frederick, G.M. McClelland, P. Brumer, J. Chem. Phys. 83 (1985) 190.
[19] R. Prosmiti, S.C. Farantos, H.S. Taylor, Mol. Phys. 82 (1994) 1213.
[20] T.H. Dunning Jr., R.C. Raffenetti, J. Phys. Chem. 85 (1981) 1350.
[21] R.O. Jones, J. Chem. Phys. 82 (1985) 325.
[22] G.B. Bacskay, A.P.L. Rendell, N.S. Hush, J. Chem. Phys. 89 (1988) 5721.
[23] K. Kamiya, H. Matsui, Bull. Chem. Soc. Jpn. 64 (1991) 2792.
[24] C.B. Kellogg, H.F. Schaefer III, J. Chem. Phys. 102 (1995) 4177.
[25] J.M.L. Martin, J. Chem. Phys. 108 (1998) 2791.
[26] P. Nachtigall, J. Hrusák, O. Bludský, S. Iwata, Chem. Phys. Lett. 303 (1999) 441.
[27] S.P.J. Rodrigues, J.A. Sabín, A.J.C. Varandas, J. Phys. Chem. A, in press.
[28] A.J.C. Varandas, Adv. Chem. Phys. 74 (1988) 255.
[29] A.J.C. Varandas, in: A. Laganá, A. Riganelli (Eds.), Reaction and Molecular Dynamics. In: Lecture Notes in Chemistry, vol. 75, Springer, Berlin, 2000, p. 33.
[30] S.C. Farantos, E.C. Leisegang, J.N. Murrell, J.J.C. Teixeira-Dias, A.J.C. Varandas, Mol. Phys. 34 (1977) 947.
[31] S. Carter, I.M. Mills, J.N. Murrell, A.J.C. Varandas, Mol. Phys. 45 (1982) 1053.
[32] J.N. Murrell, W. Craven, M. Vincent, Z.H. Zhiu, Mol. Phys. 56 (1985) 839.
[33] A. Bastida, J. Zúñiga, A. Requena, J. Mol. Spectrosc. 136 (1989) 185.
[34] E. Kauppi, L. Halonen, J. Chem. Phys. 96 (1992) 2933.
[35] B. Weis, PhD thesis, University of Frankfurt, Frankfurt, Germany, 1991.
[36] H. Müller, H. Köppel, Chem. Phys. 183 (1994) 107.
[37] G. Lendvay, G.C. Schatz, L.B. Harding, Faraday Discuss. 102 (1995) 389.
[38] B.O. Roos, K. Andersson, M.P. Fülsher, P.-A. Malmquist, L. Serrano-Andrés, K. Pierloot, M. Merchán, Adv. Chem. Phys. XCIII (1996) 219.
[39] B.O. Roos, P.E.M. Siegbahn, Plenum, New York, 1977, p. 277.
[40] T.H. Dunning Jr., J. Chem. Phys. 90 (1989) 1007.
[41] R. Kendall, T. Dunning Jr., R. Harrison, J. Chem. Phys. 96 (1992) 6769.
[42] H.-J. Werner, P.J. Knowles, MOLPRO is a package of ab initio programs written by H.-J. Werner, P. J. Knowles, with contributions from J. Almlöf, R.D. Amos, M.J.O. Deegan, S.T. Elbert, C. Hampel, W. Meyer, K.A. Peterson, R. Pitzer, A.J. Stone, P.R. Taylor, R. Lindh, 1998.
[43] A.J.C. Varandas, J. Chem. Phys. 90 (1989) 4379.
[44] A.J.C. Varandas, J.D. Silva, J. Chem. Soc. Faraday Trans. 88 (1992) 941.
[45] A.J.C. Varandas, J. Chem. Phys. 105 (1996) 3524.
[46] A.J.C. Varandas, J. Brandão, Mol. Phys. 45 (1982) 857.
[47] A.J.C. Varandas, J. Mol. Struct. Theochem 120 (1985) 401.
[48] A.J.C. Varandas, Mol. Phys. 60 (1987) 527.
[49] A.J.C. Varandas, in: G. Delgado-Barrio (Ed.), Dynamical Processes in Molecular Physics, IOP Publishing, Bristol, 1993, p. 3.
[50] A.D. Buckingham, Adv. Chem. Phys. 12 (1967) 107.
[51] A.J.C. Varandas, J. Brandão, L.A.M. Quintales, J. Phys. Chem. 92 (1988) 3732.
[52] A.J.C. Varandas, J. Mol. Struct. Theochem 166 (1988) 59.
[53] A.J.C. Varandas, A.A.C.C. Pais, Mol. Phys. 65 (1988) 843.
[54] A.J.C. Varandas, S.P.J. Rodrigues, J. Chem. Phys. 106 (1997) 9647.
[55] S.P.J. Rodrigues, A.J.C. Varandas, Phys. Chem. Chem. Phys. 2 (2000) 435.
[56] E. Martínez-Núñez, A.J.C. Varandas, J. Phys. Chem. A 105 (2001) 5923.
[57] M.R. Pastrana, L.A.M. Quintales, J. Brandão, A.J.C. Varandas, J. Phys. Chem. 94 (1990) 8073.
[58] J.J. Moré, B.S. Garbow, K.E. Hillstrom, Argonne National Laboratory, 1980; MINPACK package can be obtained from http://www.netlib.org/minpack/.
[59] J.J. Moré, in: G.A. Watson (Ed.), Numerical Analysis. In: Lecture Notes in Mathematics, vol. 630, Springer, Berlin, 1977, p. 105.
[60] G. Guelachvili, O.N. Ulenikov, G.A. Ushakova, J. Mol. Spectrosc. 108 (1984) 1.
[61] G. Steenbeckliers, J. Bellet, J. Appl. Phys. 46 (1975) 2620.
[62] G. Guelachvili, O.V. Naumenko, O.N. Ulenikov, J. Mol. Spectrosc. 125 (1988) 400.
[63] W.J. Lafferty, A.S. Pine, G. Hilpert, R.L. Sams, J.-M. Flaud, J. Mol. Spectrosc. 176 (1996) 280.
[64] W.J. Lafferty, J.-M. Flaud, G. Guelachvili, J. Mol. Spectrosc. 188 (1998) 106.
[65] J.-M. Flaud, A. Perrin, L.M. Salah, W.J. Lafferty, G. Guelachvili, J. Mol. Spectrosc. 160 (1993) 272.
[66] J.-M. Flaud, W.J. Lafferty, J. Mol. Spectrosc. 161 (1993) 396.
[67] J. Tennyson, J.R. Henderson, N.G. Fulton, Comput. Phys. Commun. 86 (1995) 175.
[68] J. Tennyson, B.T. Sutcliffe, Int. J. Quantum Chem. 42 (1992) 941.
[69] C.D. Paulse, J. Tennyson, J. Mol. Spectrosc. 168 (1994) 313.

[70] M. Menou, C. Leforestier, Chem. Phys. Lett. 210 (1993) 294.
[71] A.J.C. Varandas, Z.R. Xu, in: G.D. Billing, M. Baer (Eds.), Adv. Chem. Phys., in press.
[72] J. Tennyson, J. Chem. Soc. Faraday Trans. 88 (1992) 3271.
[73] M.A. Collins, Adv. Chem. Phys. 93 (1996) 389.
[74] T.-S. Ho, H. Rabitz, J. Chem. Phys. 104 (1996) 2584.
[75] A.J.C. Varandas, L. Zhang, Chem. Phys. Lett. 331 (2000) 474.
[76] A.J.C. Varandas, J. Chem. Phys. 107 (1997) 867.
[77] R. Prosmiti, O.L. Polyansky, J. Tennyson, Chem. Phys. Lett. 273 (1997) 107.
[78] P.J.S.B. Caridade, A.J.C. Varandas, submitted for publication.
[79] A.J.C. Varandas, S.P.J. Rodrigues, P.A.J. Gomes, Chem. Phys. Lett. 297 (1998) 458.
[80] A.J.C. Varandas, in: M. Yáñez (Ed.), Trends in Atomic and Molecular Physics, Universidad Autonoma de Madrid, Madrid, 1990, p. 113.
[81] J.P. Desclaux, At. Data Nucl. Data Tables 12 (1973) 311.
[82] A.J.C. Varandas, A.I. Voronin, Chem. Phys. 194 (1995) 91.
[83] Y. Morino, Y. Kikuchi, S. Saito, E. Hirota, J. Mol. Spectrosc. 13 (1964) 95.